Acta Astronautica 236 (2025) 746–754

Contents lists available at ScienceDirect

Acta Astronautica

journal homepage: www.elsevier.com/locate/actaastro

Research paper

Flat retroreflective arrays and foils for satellite laser ranging

Moritz Vogel *, Nils Bartels, Maximilian Feiling, Jürgen Kästel, Stefan Scharring,
Wolfgang Riede, Thomas Dekorsy

German Aerospace Center (DLR), Institute of Technical Physics, Pfaffenwaldring 38-40, Stuttgart, 70569, Germany

ARTICLE INFO

Keywords:
Satellite laser ranging
SLR
Space debris
Retroreflector
Retroreflective foil
Space traffic management
Metasurface

ABSTRACT

Retroreflective structures play an important role in laser-based space applications, serving as navigation aids for spacecraft docking and enabling precise orbit determination through satellite laser ranging. These structures must deliver a high return signal over long distances while being durable, and capable of operating in the challenging conditions of space for extended periods. Flat retroreflective structures such as retroreflective foils would be beneficial to ensure a seamless integration with various satellites, particularly CubeSats. This study analyzes the far-field diffraction patterns of various commercially available retroreflective foils, which are crucial for calculating the optical cross-section. While the retroreflected signal from these foils is notably weaker than that of conventional corner-cube retroreflectors of equivalent area, it remains several orders of magnitude stronger than that of a diffusely reflecting surface. Beyond conventional retroreflective foils, which rely on arrays of microprisms, we explore the potential of flat retroreflective structures based on metasurfaces. These nanostructures offer intriguing possibilities, such as wavelength-dependent retroreflection, and may be engineered for compatibility with space environment. In the future, such advanced designs could enable innovative applications like satellite identification or attitude determination. Moreover, we theoretically analyze how the changing attitude of the satellite affects the return signal of potentially coherently retroreflecting arrays.

1. Introduction

The growing number of satellites and space objects necessitates improved tracking, monitoring, and management systems to ensure the safety of space operations. These activities, collectively known as Space Traffic Management (STM), are becoming increasingly critical. Satellite Laser Ranging (SLR), a well-established technique in space geodesy [1], has been proposed for use with non-geodetic targets to achieve precise orbit determination. In scenarios involving close conjunctions between space objects, SLR-derived orbit data can enhance collision risk assessments, potentially reducing the frequency of costly collision avoidance maneuvers [2]. Additional applications of laser ranging in space include precise distance measurements during docking maneuvers and laser-based 3D positioning, achieved by ranging to multiple retroreflectors on space objects using scanning LiDAR systems [3,4]. For an effective exploitation of SLR for space traffic management, it would be highly advantageous, if an increasing number of space objects were equipped with retroreflective devices. In a study on "Innovative methods for trackability and identification improvement of small objects for space traffic management" ESA currently mentioned the approach of using retroreflective foils for tracking as 'an alternative technology, which is currently under study' [5]. And in recent work, retroreflective foils have also been suggested to be mounted to satellites for SLR and successful ground-based field tests over a range of 30 km have been conducted [6]. This motivated the planning of an upcoming space mission in which a 3U CubeSat will be equipped with retroreflective foil for ranging with ground based SLR stations [7]. Such retroreflective foils would not have a very precise invariant point of retroreflection and are thus not suitable for geodetic, mm-precision SLR, but the achievable ranging accuracy would still be sufficient for space traffic management. The idea to use retroreflective foils for ranging over long distances (e.g. 600 km in a typical low Earth environment) in space brings several technical challenges and research questions. Particularly, the foil would be operating in a challenging space environment, which can exhibit rapid changes of temperature, degradation due to space radiation (protons, electrons) and UV light, as well as atomic oxygen. Another major topic that has not yet been adequately discussed in previous work is the link budget of laser ranging to satellites equipped with retroreflective foils, which strongly depends on the diffraction of retroreflected light. Since retroreflective foils consist of multiple small micro-prisms, they are expected to have a broader far-field diffraction pattern (FFDP)

---

* Corresponding author.
E-mail address: moritz.vogel@dlr.de (M. Vogel).

https://doi.org/10.1016/j.actaastro.2025.07.021
Received 30 January 2025; Received in revised form 18 March 2025; Accepted 9 July 2025

compared to a conventional single (larger) retroreflector. In this work we analyze the FFDP of commercial retroreflective foils and calculate the resulting optical cross-section. Based on this analysis, we discuss the feasibility of using retroreflective foils for satellite laser ranging. In addition to conventional retroreflective foils, we also discuss the opportunity of using flat retroreflective metasurfaces. Retroreflective metasurfaces use sub-wavelength structures and have interesting properties such as a strong dependence of retroreflection on wavelength and angle. Furthermore, they are manufactured using sub-nanometer precision lithography processes with few (often inorganic) materials, which might enable an efficient and space compatible manufacturing. Notably, they already are considered for multiple applications in space such as solar sails [8], solar reflectors [9], antennas [10] and space based imaging systems [11]. The sub-wavelength structures manufactured by high accuracy processes might also enable a coherent return. For free space optical communication first simulations of returned power of micromachined corner cube retroreflectors (CCRs) with respect to non-idealities have been performed [12]. However, for the purpose of SLR with dynamic satellite attitude, additional implications emerge, which we discuss based on simulations of the far-field diffraction pattern.

This article is structured as follows. The next section explains the importance of the FFDP for the signal strength of retroreflector arrays in SLR experiments. Section 3 describes experimental results (FFDPs, reflectivity and a microscopic characterization) of several commercial retroreflective foils. These results are then used to compute optical cross sections (OCS) of retroreflective foils (Section 4). Section 5 describes opportunities of coherent retroreflective arrays followed by a summary and conclusions (Section 6).

2. Importance of the far-field diffraction pattern of retroreflector arrays for SLR experiments

Fig. 1 shows a schematic of a SLR experiment. An SLR station emits laser pulses towards a satellite which is equipped with a retroreflector (or an array of retroreflectors). A retroreflector typically consists of three mutually perpendicular rear faces, which serve as reflective surfaces. By reflecting the incoming beam at each of those perpendicular surfaces, the velocity vector is reversed across a broad range of incidence angles (AOI) and thus redirected towards the ground station. The distance from the ground station to the retroreflector is derived by measuring the two-way photon travel time of laser pulses. These precise distances can then be used for orbit refinement.

A prerequisite for successful ranging experiments is a sufficient photon detection rate of incoming retroreflected laser light. This SLR return rate (photons per emitted laser pulse) depends on several factors including the outgoing laser pulse energy and beam divergence, the size of the receiving telescope and the efficiency of the receiving (often single photon counting) detector [13]. Of course, another important factor is the optical cross section σ of the retroreflector (array). In the far-field limit, this optical cross section (in units of square meters) strongly depends on the beam divergence of light that is reflected from the retroreflector (array). Therefore, the received intensity in the far-field is directly proportional to the transmitted intensity and the optical cross-section, but inversely proportional to the square of the distance traveled. Methods for calculating the optical cross section have been developed since the beginning of SLR technology development [14]. A typical approach for the calculation is to approximate each retroreflector simply as an aperture. This approximation is based on the fact that an ideal (perfectly manufactured retroreflector) has identical path lengths for all retroreflected rays. The peak (on-axis) cross section for an incidence angle of 0° of a perfect retroreflector with an area A_{CCR} can be written as

$$\sigma_0 = \rho_{CCR} \cdot \frac{4\pi A_{CCR}^2}{\lambda^2} \tag{1}$$

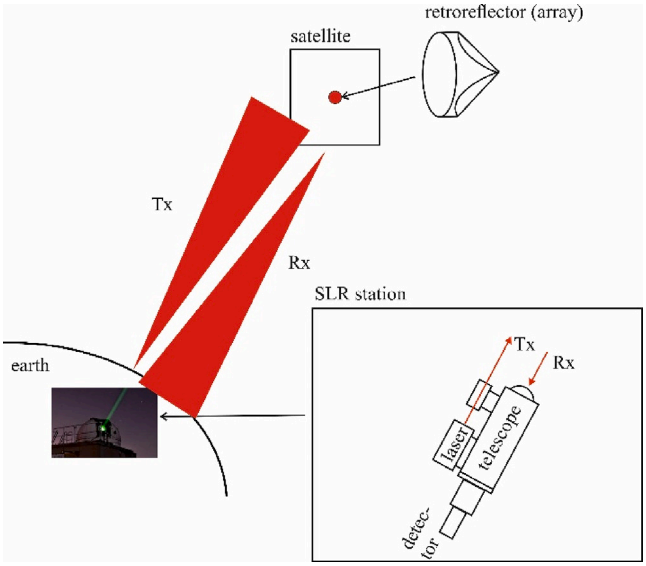

Fig. 1. Schematic of a satellite laser ranging (SLR) experiment. The signal strength of laser pulses detected after retroreflection strongly depends on the diffraction pattern (beam divergence) of the retroreflected beam.

where ρ_{CCR} is the reflectivity, and λ is the SLR wavelength. The reason that the cross section increases with the square of the retroreflector area is that a decrease of the aperture size will not only reduce the fraction of the beam emitted at the SLR station that hits the retroreflector, but additionally generate a broader beam divergence of retroreflected light.

In this work, we are considering retroreflective foils, which consist of many small retroreflecting substructures (typically $D_{sub} < 500$ µm diameter, listed in Table 1) and thus represent an array of retroreflectors.

The diffraction pattern in the observation plane (x', y') at z' for a single aperture in the aperture plane (x, y) at z in the far-field limit is given by the Fraunhofer diffraction equation [15] as

$$E(x', y', z') = \frac{e^{ikz'}}{i\lambda z'} \iint_{\Omega} e^{-\frac{ik}{z'}(xx'+yy')} \cdot E_{\text{aperture}}(x, y)\, dx\, dy \tag{2}$$

where $k = 2\pi/\lambda$ is the wavenumber, λ the wavelength and $E_{aperture}$ the electric field distribution in the aperture plane.

Furthermore, we describe the aperture function of an array of N identical apertures with centers located at (x_n, y_n) via the sum

$$E(x, y) = \sum_{n=1}^{N} E_{\text{aperture}}(x - x_n, y - y_n) \cdot e^{i\phi_n} \tag{3}$$

where we have introduced a piston phase distortion ϕ_n for each individual aperture. These different phase distortions can either be used to describe the irradiation of an array at non-normal incidence angle (in which case the phases would be different due to different path lengths for the rays before entering and after leaving the different apertures) or manufacturing errors (which would randomly change the phases).

Retroreflective foils are micro-structured arrays of retroreflectors with typically hexagonal output apertures [16]. For these technical products one can assume that the variation of the optical path lengths inside the different subunits is much larger than the wavelength. In this case, the far-field diffraction pattern of an array with a large number of individual retroreflective units would be incoherent and thus identical to the FFPD of these units and the optical cross section (OCS) of the array $\sigma_{0,\ total}$ is given by the OCS of the single unit σ_0 multiplied with the number of units n in the array [9].

$$\sigma_{0,total} = n \cdot \sigma_0 \tag{4}$$

Table 1

Summary of foil analysis, including diffraction angle Θ and reflectivity ρ_{CCR} for foils with a diameter of sub-units D_{sub}. For foil 2–6 it was not possible to unambiguously determine a first minimum and an associated diffraction angle, however it was apparent that the angle is larger than theoretically estimated (compare Fig. 3d)).

Label	Type	D_{sub} [µm]	Θ_{theory} [mrad]	$\Theta_{measured}$ [mrad]	ρ_{CCR} (0° AOI)
Orafol VC170	Triangular	67	12.65	12.9	0.33
IMOS M120-24	Hexagonal	345	2.46	>2.46	0.39
IMOS F056	Triangular	100	8.47	>8.47	0.38
3M 4090	Full-cube	140 × 100	7.1[a]	>7.1	0.91
IMOS M149-20	Hexagonal	462	1.84	>1.84	0.39
Orafol OR6910	Triangular	100	8.47	>8.47	0.62

[a] Estimation with the simplification of computing a hexagonal aperture with an averaged diameter of 120 µm.

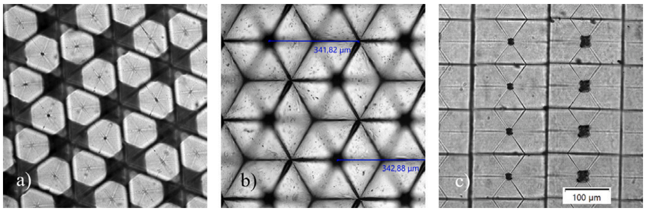

Fig. 2. DICM images of different types of retroreflective micro-prisms. (a) triangular (Orafol VC170), (b) hexagonal (IMOS M120-24), (c) full-cube (diamond-grade) (3M 4090).

In practice, the OCS is diminished due to a reduction in the effective receiver area, which results from varying incidence angles, as well as a shift in the relative position of the ground station with respect to the satellite (velocity aberration). Therefore, a more accurate estimation of the OCS can be achieved by calculating the mean OCS (for these computations a maximum angle of 35° was considered). All values are derived based on John Degnan's review on millimeter accuracy satellite laser ranging [13].

3. Characterization of commercial retroreflective foils

Retroreflective foils are widely used and analyzed for ground applications such as traffic management with short slant ranges [17–19]. For further analysis in the context of SLR, where the slant ranges are considerably larger, we measured the FFDP of several commercially available retroreflecting foils and compared them to numerical simulations [20]. Diffraction patterns were measured in a laboratory setup using a continuous-wave Helium Neon (HeNe) laser operating at a wavelength of $\lambda = 632$ nm. Experimental details are provided in Appendix A.

Table 1 provides an overview of results for the reflectivity and diffraction characteristics of different commercial retroreflective foils. These foils have different designs of the microstructures that generate retroreflection and depending on the design the effective aperture of each subunit can be either triangular, hexagonal or cubic. Fig. 2 shows images of different retroreflective foils taken via differential interference contrast microscopy (DICM). Fig. 2(a) depicts the triangular design, where 1/3 of the area cannot contribute to retroreflection, thus the effective output aperture is hexagonal. In exchange, this type is the simplest to manufacture. Fig. 2(b) shows the truncated, hexagonal design and Fig. 2(c) shows the full-cube design (also known as Diamond Grade). This full cube-technology uses a clever re-shape to achieve maximum reflectivity in combination with a maximized fill-factor [21].

We have measured the shape and dimensions of each microstructure via DICM and results are provided in Table 1. This information was then used to compute the FFDPs as described in the previous section, as well as a 'theoretical diffraction angle' (provided for the tested wavelength of 632 nm and given in Table 1), which is the first minimum of the radial distribution in the FFDP.

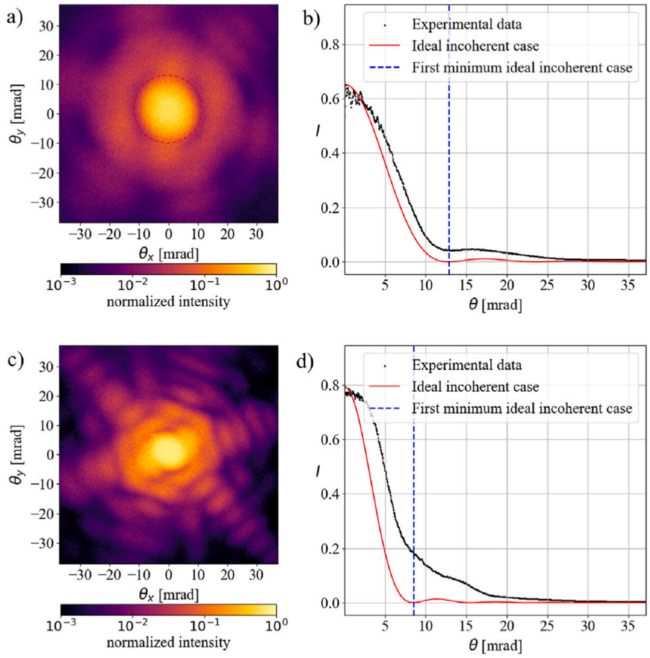

Fig. 3. Diffraction analysis of Orafol ORALITE VC170 (a, b) and of IMOS F056 (c, d) retroreflective foil. Recorded spatial distribution of normalized intensity (a, c) and radially averaged intensity profile (b, d). Red dashed circle indicates first minimum of the FFDP (only for (a), since in (c) it was not possible to unambiguously determine a first minimum).

These calculated diffraction patterns can then be compared to experimental data. Fig. 3 shows a comparison between measured and calculated FFDPs of two different retroreflective foils. The top panels show results for the retroreflective foil Orafol ORALITE VC170, made for emergency vehicles. The typical 'star'-shaped FFDP of a hexagonal output aperture is clearly visible in the logarithmic plot of Fig. 3(a). Fig. 3(b) displays a cross section of the intensity across the pattern (radially averaged). A distinctive first minimum is observable at approximately 12.9 mrad. This corresponds very well with the theoretical minimum of hexagonal apertures with an outer diameter of 67 µm (12.65 mrad). Panels (c) and (d) of Fig. 3 show results for the IMOS F056 foil. Similar to most other foils, the measured diffraction pattern was significantly broader than expected from the modeling of the apertures. Moreover, it was not possible to unambiguously determine a first minimum and an associated diffraction angle. Both outcomes are presumably due to manufacturing errors (e.g. dihedral angle offsets, curvature or nonflatness) in the substructures. In any case, the modeling of the diffraction via the area of the individual micro-prisms in the foils provides a lower limit for the broadening of the retroreflected beam.

Table 2
Overview on mean optical cross section averaged between −35° and +35 assuming a reflectivity of 0.9. To put this into context of current missions, examples for each CCR diameter were added. Information on retroreflectors of past and active missions can be found at the International Laser Ranging Service (ILRS) [22].

Diameter [mm]	Mean cross section [m^2 sr^{-1}]	Examples
10	23 604	TUBIN
12.7	54 800	–
28.2	459 097	Galileo, Glonass
33	573 653	Galileo
38	667 512	Champ, Grace-FO, Swarm, Apollo

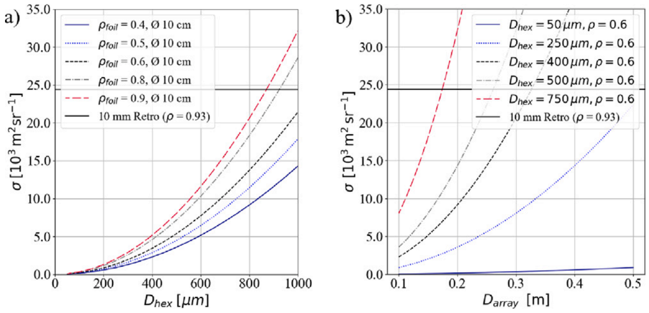

Fig. 4. (a) Optical cross section as a function of the size of a single corner cube and the reflectivity (constant size of foil), (b) OCS as a function of the reflective area and the size of a single corner cube (constant reflectivity). The OCS of a 10 mm corner cube serves as a benchmark.

4. Derivation of the optical cross section for retroreflective foils

Based on this knowledge, we can assess the optical cross-section and leverage these insights to evaluate feasibility and providing valuable guidelines for design decisions. There are three major parameters which can be varied or vary depending on the foil. This is the reflectivity, the size of a single corner cube in a foil (determining the diffraction behavior) and the size of the foil itself (in this study always outlined as diameter of a circular area). Triangular foils are by design limited to a maximum of 67% reflectivity [16], thus hexagonal or full-cube structures are advantageous in theory. Therefore, the following featured figures only consider hexagonal structured foils. Our experimental results show that for the most foils the diffraction angle is much larger than theoretically expected, however for one foil it matched very well. Thus, with current technology it seems to be possible to get close to this limit and the following calculations consider this case.

Fig. 4 represents the results of a parameter study examining the OCS σ with regards to the previously identified key parameters. Fig. 4(a) shows the variation of the OCS due to an increase of the size D_{Hex} of the micromachined hexagonal corner cubes in the array and a variation of the reflectivity (the array's dimensions are fixed at a diameter of 10 cm, which corresponds to the available area on a 1U CubeSat). Obviously, due to the quadratic nature of Eq. (1), an increase of the unit-size has a significant impact on the OCS. Thus, with typical retroreflective foils (~400 μm) it is not possible to achieve a comparable OCS as a 10 mm single CCR (backcoated) on a 1U CubeSat.

The 10 mm single CCR has been chosen as a comparative figure since it is used for our own CubeSat dedicated developments and also can be found on CubeSats such as TUBIN of TU Berlin. However, to put the cross section into a broader context it can be compared to other CCRs on current missions presented in Table 2.

Considering the available area and assuming a high reflectivity, the unit size needs to be increased to ~870 μm (ρ = 0.9) or ~920 μm (ρ = 0.8). However, in this case it is questionable if the flexible properties of a foil can be preserved. Fig. 4(b) shows the variation of the OCS if the available area is varied. From this, it can be derived that for a typical retroreflective foil (~400 μm) and a medium reflectivity of 0.6 a reflective area with diameter of ~33 cm is required to match the OCS of the 10 mm single corner cube. For even smaller unit sizes, the required area is increased drastically.

5. Case study for a coherent retroreflective array based on metasurfaces

The commercial retroreflective foils analyzed in this work did not show a coherent retroreflection from the different microprisms in the foil and it was also inconceivable for an array of mm to cm sized CCRs in the past. However, this incoherent return results in a high diffraction angle, which ultimately leads to an increased area required on the satellite. This of course brings up the question, whether flat retroreflective devices with a high optical cross section could be manufactured, in which different retroreflecting substructures provide a high SLR signal strength due to constructive interference. In the last decades, the invention of metasurfaces, which are artificial, nanostructured surfaces introduced a novel way to modulate electromagnetic waves [23]. Due to its nature, the surfaces have to be structured on the sub-wavelength scale, e.g. by lithographic manufacturing processes. Arbabi et al. already created a retroreflective metasurfaces for a wavelength of 850 nm and minimized the wavefront error of single cell to <0.005 rad root-mean-square (RMS) wavefront error up to an AOI of 10° [24]. It also achieves a reflectivity of approximately 78% at its specifically designed wavelength. Enhancing the efficiency of metasurfaces is currently an active area of research. Nevertheless, this result already approaches the reflectivity performance of total internal reflection corner-cube retroreflectors, which typically reach a reflectivity of about 93%, accounting for losses at the front surface and within the bulk material. It also comes close to aluminum-back-coated retroreflectors, which exhibit reflectivities of approximately 85%, although the precise values depends on the wavelength. While the working principle is totally different compared to classical optics, it is just another way to create a custom lens and a custom mirror. However, the published results consistently reflect the reflection of a single cell. In this case, each hexagonal unit cell is 600 μm in diameter and only has a thickness of ~500 μm. Thus, this also needs to be modeled as an array of unit-cells. Indeed, Suo et al. recently created another wide-angle flat reflector based on a metalens and a flat metallic reflector which is considerable larger (up to 8 cm in diameter) [25]. However, this results in a much thicker reflector of 3 cm. So, if the flat and thin property shall be preserved, an array of retroreflective unit cells is still inevitable. Nonetheless, the sub-nm precision of lithographic processes might offer the possibility to manufacture constructively interfering, flat retroreflective devices in the future. It is also known, that it is possible to establish workflows for fabricating wafer-scale metalenses using deep-ultraviolet photolithography [26], which in this case was demonstrated for an 80 mm aperture metalens telescope.

As stated above, a prerequisite to achieve constructive interference is a low manufacturing tolerance. Thus, we started by evaluating the required manufacturing tolerance by simulating the misalignment of sub-apertures and the resulting FFDP. For this purpose, we have modeled a specific retroreflector array. The structure of this array is depicted in Fig. 5, which is constructed out of 91 hexagonal apertures with an outer radius of 500 μm to optimally fill a 10 mm sized array.

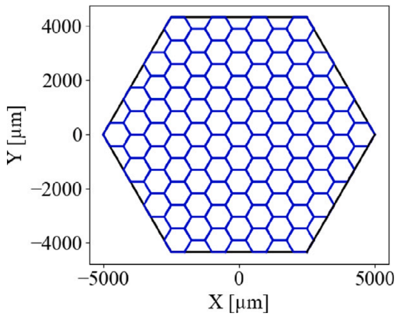

Fig. 5. Structure of the considered array of hexagonal retroreflective unit cells. The array itself is shaped hexagonal as well.

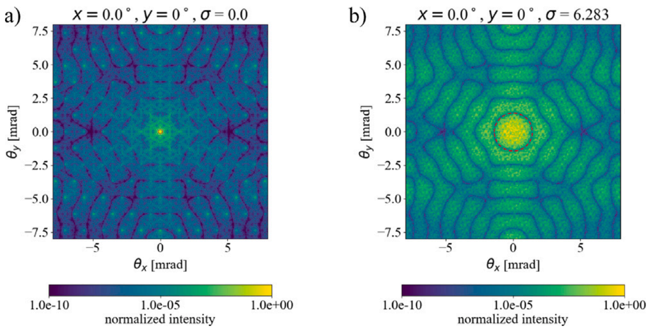

Fig. 6. Far-field diffraction patterns of a hexagonal array consisting of hexagonal sub-apertures. (a) FFDP of an ideal array, (b) FFDP of an array with misalignment of the sub-apertures simulated by introducing phase noise of 2π. x and y in the header specify the tilt around the x-axis respectively the y-axis and σ the standard deviation of a Gaussian distribution in rad. Red dashed circle indicates first minimum of the FFDPs.

Fig. 6 shows the calculated FFDP of this retroreflector array when irradiated with a laser (at a wavelength of 1064 nm, which is a typical SLR wavelength [27]) at normal incidence. Panel (a) of Fig. 6 shows the FFDP assuming a perfectly manufactured array. In this case, constructive interference would lead to a very narrow FFDP, where the first minimum of the diffraction angle occurs at 0.17 mrad (~100 m radius on the ground for an altitude of 600 km). Of course, this constructive interference would degrade in case of a phase noise (e.g. introduced by manufacturing tolerances). Panel (b) of Fig. 6 shows the FFDP of an array with misalignment of the sub-apertures simulated by introducing phase noise of 2π (a full wave). In this case, an incoherent return is obtained. We have analyzed that a manufacturing tolerance (variation of the position coordinates of the corner positions of hexagons in the array) on the order of ~90 nm (at a wavelength of 1064 nm) would be required to achieve a peak intensity of 75% of the ideally manufactured array. Details on this analysis are provided in Appendix B.

Typically, metasurfaces are manufactured by UV-lithography or nanoimprint lithography [28]. Deep-UV lithography manufacturing processes can produce metasurfaces with diffraction-limited behavior [29] and have typical process nodes (typically describes the minimum feature size or transistor density achievable) far below 100 nm and line edge roughness's of 2.7 nm (3σ) [30]. For those types of manufacturing techniques, the mentioned performance indicators are more frequently used than 'manufacturing tolerance', nonetheless a node size of 100 nm requires a manufacturing tolerance considerably beneath the defined requirement. Applying nanoimprint lithography processes is also highly favorable for large-scale manufacturing of metasurfaces that consist of nanostructures <100 nm [31].

From this perspective it might be in the realm of possibility to realize coherently retroreflective surfaces using this technology. However, it is known that e.g. phased radar arrays or coherent coupled lasers exhibit effects such as beam steering [32]. The term 'beam steering' typically refers to the controlled redirection of a laser beam e.g. by a phased array using constructive and destructive interference. An unintentional phased array due to a tilt of the satellite might thus lead to a displacement of the beam and adversely impact SLR. Thus, we used the model to assess the implications. And unfortunately, as described in more detail in Appendix C, a tilt of the retroreflector array irradiated on a 600 km distance LEO satellite would indeed induce a maximal displacement of the beam on Earth of ~650 m. To put the impact of potential beam steering into context, it can be compared to another phenomenon which causes a displacement of the beam during SLR, which is the velocity aberration. This term describes the displacement due to the relative movement of the satellite relative to the incoming laser beam during SLR. For a satellite with an altitude of 600 km and a station latitude of 48.78° (location of miniSLR® in Stuttgart, Germany) this causes a velocity aberration of approximately 10 arcsec which corresponds to ~30 m (further depending the zenith angle of observation) [33]. Thus, the impact of beam steering is an order of magnitude larger than the velocity aberration and would thus have a detrimental effect, since the signal cannot always be received at the station. Therefore, a coherent retroreflective array would only provide a significantly improved signal strength in SLR, if the array was fine pointed with high precision (on the order of ~100 arcsec) with respect to the ground station. By now modern attitude and orbital control systems (AOCS) enable outstanding pointing accuracy and pointing stability. For example, the AOCS of the Euclid satellite (part of ESA Cosmic Vision program) achieves a relative pointing error of less than 25 milliarcseconds (1σ) over 700 s [34]. Also satellites which are considered as rather low-budget such as the 'Flying Laptop' of University of Stuttgart (150 arcsec) can almost fulfill these requirements [35]. For CubeSats it can be referred to DLR's Optical Communication Terminals for CubeSats, which use a 4-Quadrant Diode to measure the angular error of the pointing and apply this information to readjust a fast steering mirror [36]. These terminals have a pointing accuracy of at least ±0.1° (360 arcsec) and thus already come close to the required pointing accuracy for the mitigation of beam steering on a CubeSat platform. The signal of this technique could also be used to control an actuator to readjust the pointing of such an array.

While this analysis especially discussed the impact on a LEO satellite with an altitude of 600 km, it is worth briefly considering the implications of these findings for other scenarios. From a theoretical view, the central maximum of the FFDP and the beam steering are both characterized by an angle originating from the same source (the retroreflecting array). Thus, the ratio of their overlapping area to the total area remains independent of distance. This means, that the beam steering problem is independent of the orbital height, or in other words, the ratio of scenarios where a signal can be received to the ones where the beam is steered out of the receiving area remains independent of distance, at least as long as the far-field requirement is fulfilled.

6. Summary and conclusions

In general, commercial of-the-shelf (COTS) retroreflective foils and microprisms show diffraction angles worse than the ideal incoherent case suggesting further non-idealities such as dihedral angle offsets, curvature or nonflatness. However, one of the tested foils achieved results close to the diffraction limit of the incoherent case. In addition, all foils have a rather low reflectivity around 40% with the exception of full-cube foils (91%). The provided parameter study shows which set of parameters is required to achieve a certain required optical cross section. From this, the performance of COTS foils could be derived, but it also serves as a tool to identify requirements or targets for potential SLR dedicated developments. For example, a slightly higher diameter of a single unit might be advantageous especially in the context of SLR, but has to be balanced out with further requirements such as flexibility. To make the rather complex results more accessible, Fig. 7 breaks down the results to one exemplary key result. It illustrates

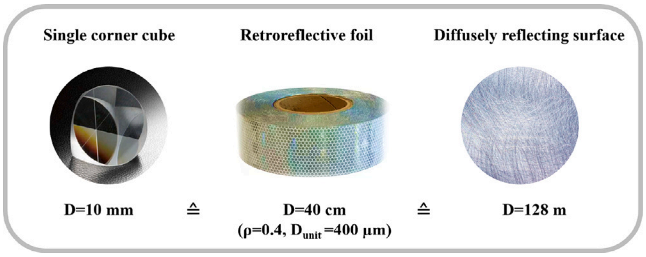

Fig. 7. Descriptive comparison of required reflective areas (circular areas with a diameter D) of single corner cube retroreflectors (backcoated), retroreflective foils and diffusively reflecting surfaces to achieve an identical optical cross section.

how large the reflective areas need to be in order to achieve a similar OCS for each approach. The 10 mm single CCR serves as a benchmark since it can still be observed using the miniSLR® (operated at DLR in Stuttgart) [27]. To achieve the same OCS, a COTS foil with an almost ideal diffraction behavior would require a circular area with a diameter of at least 40 cm, while a diffusively reflecting surface would require a diameter of 128 m. Considering those results an average COTS foil might require a reflective area which might not be suitable for most applications, but still represents a massive improvement compared to a diffusively reflecting surface.

Constructive interference of substructures in a flat retroreflective array manufactured with high precision, might be a way to further increase the SLR signal strength.

This means, that an ideal coherently reflecting array with minimized spacing would approximately generate the diffraction angle of a single conventional back coated retroreflector of the same size. The reason is that in that case, both, an ideal coherently reflecting array and an ideal back coated corner cube reflector would be diffraction limited by their outer diameter (this is different for TIR retroreflectors). Thus, the potential of a coherently reflecting array is to achieve the same narrow diffraction angle, while the aperture diameter is geometrically decoupled of the height. Unfortunately, at the cost of beam steering. The manufacturing of such arrays might be possible in the future (e.g. using metamaterials manufactured via lithography), but would require fine pointing of the array towards the SLR ground station to avoid unwanted effects of beam steering. Such pointing stability can be achieved with today's attitude and orbital control systems (AOCS) [34], though this requires an active satellite, which prevents coherent SLR for passive or in-active satellites. Therefore, this might be of interest for applications which comprise of an active component or have access to the pointing of the satellite. Of course, the impact of further non-idealities, temperature effects and atmospheric disturbances has to be considered in further analyses and eventually a proof of feasibility has to be provided experimentally. Especially atmospheric turbulences can impact the wavefront phase and link budget of SLR [37].

Another important consideration is the question of how flat retroreflective structures (e.g. foils) can become space compatible. In addition to rapid changes in temperature, degradation due to atomic oxygen and UV light, a major challenge is space radiation. Space radiation can reduce the transmission or change the refractive index of optical materials, since intrinsic radiation defects may absorb light [38,39]. The effect of space radiation on several polymers is even more detrimental, where exposure may result in modification of the chemical, thermal, optical and other surface properties [40]. In addition, the careful selection of optical coatings is important for long-term application of optical devices in space. For example, metal oxide materials such as ZrO_2, TaO_5, HfO_2 or SiO_2 have very large band gaps and thus a high transmission for short to near-UV radiation and are therefore much less susceptible to damage from ionization and UV radiation [41].

From this point of view, metasurfaces might be interesting as well, since they can be manufactured from a wide choice of materials including metals (Au), several dielectrics (e.g TiO_2, SiO_2), as well as semiconductors (GaN) [28]. Another interesting property of retroreflectors based on metamaterials is that they have a strong dependence of their optical parameters (e.g. the reflectivity) on the wavelength and laser polarization. Moreover, an electrically switchable, compact metasurface is currently under investigation [42]. This might for example be used for the identification [43,44] and attitude determination [45] of satellites, which is an important emerging topic in space science and typically require the differentiation of signal coming from individual retroreflector units.

CRediT authorship contribution statement

Moritz Vogel: Conceptualization, Writing – original draft, Visualization, Data curation, Validation, Investigation, Software, Methodology, Formal analysis. **Nils Bartels:** Supervision, Project administration, Funding acquisition, Writing – review & editing, Conceptualization. **Maximilian Feiling:** Investigation, Visualization, Software, Writing – review & editing. **Jürgen Kästel:** Methodology, Writing – review & editing, Validation. **Stefan Scharring:** Writing – review & editing, Supervision, Methodology. **Wolfgang Riede:** Writing – review & editing, Project administration, Funding acquisition, Supervision. **Thomas Dekorsy:** Supervision, Resources, Writing – review & editing, Funding acquisition.

Declaration of competing interest

The authors declare that they have no known competing financial interests or personal relationships that could have appeared to influence the work reported in this paper.

Acknowledgments

The research was funded internally by Deutsches Zentrum für Luft- und Raumfahrt e.V. (501100002946).

Appendix A

A laser-based (HeNe $\lambda = 632$ nm, continuous-wave, Spectra Physics®) test setup was used to measure the FFDP (see Fig. 8). A 20x Galilean beam expander expands the beam to illuminate an area of 20 mm diameter. This ensures that a multitude of single apertures is covered and contribute to the FFDP. It is important to ensure a collimated beam since a considerable beam divergence adversely affects the measurement of the diffraction angle. The retroreflected light is then projected on the screen in a distance $d = 4.32$ m. This approach fulfills the Fraunhofer condition ($D_{sub}^2/(\lambda \cdot d) \ll 1$), which ensures that the far-field approximation is valid. In addition, reflectivity is measured by placing a power detector directly behind the beam splitter and measuring the reflected intensity at 0° AOI.

A.1. Calibration and error margins

The reflectivity measurement is calibrated by measuring the reflected intensity I_{ref} of an optics with known reflectivity R_{ref}. For this purpose, we used an uncoated total internal reflection (TIR) corner cube reflector (Thorlabs, reflectivity at 633 nm $R_{ref} = 0.92$). The unknown reflectivities of foils and microprisms were then determined using the ratio described by Eq. (5).

$$R_{foil} = R_{ref} \cdot \frac{I_{foil}}{I_{ref}} \tag{5}$$

A PD300-UV silicon photodiode sensor was used to measure the intensity. The error of this sensor is specified with ±3% of the reading value. For the calibration of the FFDP measurements we prepared an image with vertical dark lines with a fixed distance of 2.5 mm in between. After recording calibration images, the distance between the centers of the lines were computed in pixels. The resulting pixel resolution was determined to be (0.0962 ± 0.0034) mm [20]. Consequently, the relative error is $\pm 3.5\%$. We used the Fujifilm XE-2 camera with an image resolution of 4.896×3.264 pixels.

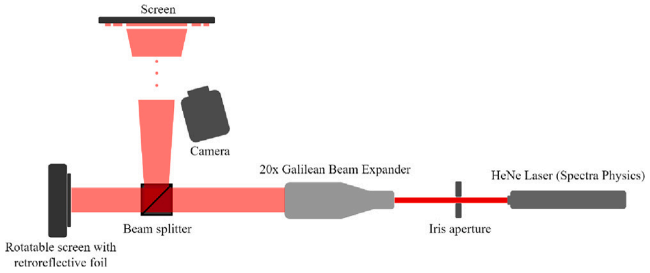

Fig. 8. Test setup for the analysis of the far-field diffraction pattern of retroreflective foils and microprisms.

Appendix B

After substituting the aperture term in Eq. (2) with Eq. (3) and further transforming the formula the full equation for far-field diffraction of an array is obtained (Eq. (6)). This equation is evaluated for the simulation results provided in this study.

$$E(x',y',z') = \frac{e^{ikz'}}{i\lambda z'} \cdot \sum_{n=1}^{N}\left(e^{i\phi_n} \cdot e^{-\frac{ik}{z'}(x_n x' + y_n y')}\right) \cdot \iint_{\Omega} E_{\text{aperture}}(x,y) \cdot e^{\frac{ik}{z'}(xx'+yy')}\,dx\,dy \tag{6}$$

For a better overview this can be subdivided in a term reflecting the array E_{grid} (Eq. (7)), a term reflecting the diffraction of a single aperture $E_{element}$ (Eq. (8)) and a constant prefactor describing the wave propagation

$$E_{\text{grid}}(x',y',z') = \sum_{n=1}^{N} e^{i\phi_n} \cdot e^{-\frac{ik}{z'}(x_n x' + y_n y')} \tag{7}$$

$$E_{\text{element}}(x',y',z') = \iint_{\Omega} E_{\text{aperture}}(x,y) \cdot e^{\frac{ik}{z'}(xx'+yy')}\,dx\,dy \tag{8}$$

Considering this, Eq. (6) can be written as

$$E\left(x',y',z'\right) = \frac{e^{ikz'}}{i\lambda z'} \cdot E_{\text{grid}}\left(x',y',z'\right) \cdot E_{\text{element}}\left(x',y',z'\right) \tag{9}$$

Manufacturing tolerances are considered by applying Gaussian noise to the piston phase. The noise or rather the standard deviation of the gauss distribution is increased stepwise up to 2π rad. For each emerging FFDP the maximum intensity is evaluated and plotted over the Gaussian standard deviation (see Fig. 9). Thus, this graph shows how the maximum return signal decreases due to degradation of coherence resulting from phase inconsistencies. Since this is a numerical evaluation, the resulting graph is subject to Gaussian noise as well and overlays the trend of decreasing maximum return signal. If a criterion for a minimum signal increase is created, a maximum manufacturing tolerance can be derived. For example, to achieve at least 75% signal strength of the coherent case, a maximum phase distortion of 0.55 rad can be tolerated. Considering the wavelength of the ground station (in this case 1064 nm), this corresponds to 93 nm.

Appendix C

The term 'beam steering' typically refers to the controlled redirection of a laser beam e.g. by a phased array using constructive and destructive interference. However, in this case an unintentional phased array emerges due to a tilt of the satellite, causing a deviation in the diffraction pattern.

Fig. 10(a)–(d) shows FFDPs for a tilt along the x-axis. For very small angles the central maximum is steered off-center along the y-axis (see Fig. 10(a), (b)). With an increasing angle two additional peaks develop as a result of constructive interference at the opposite edge of

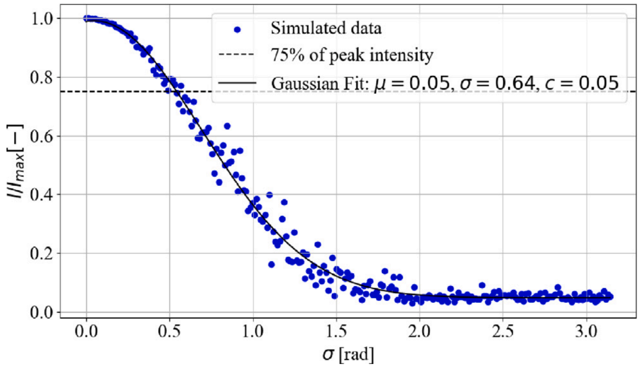

Fig. 9. Loss of peak intensity due to phase distortions induced by misalignment or manufacturing tolerances. The numerical data is fitted with a Gaussian distribution, where μ is the mean, σ the standard deviation and c an offset in y-direction.

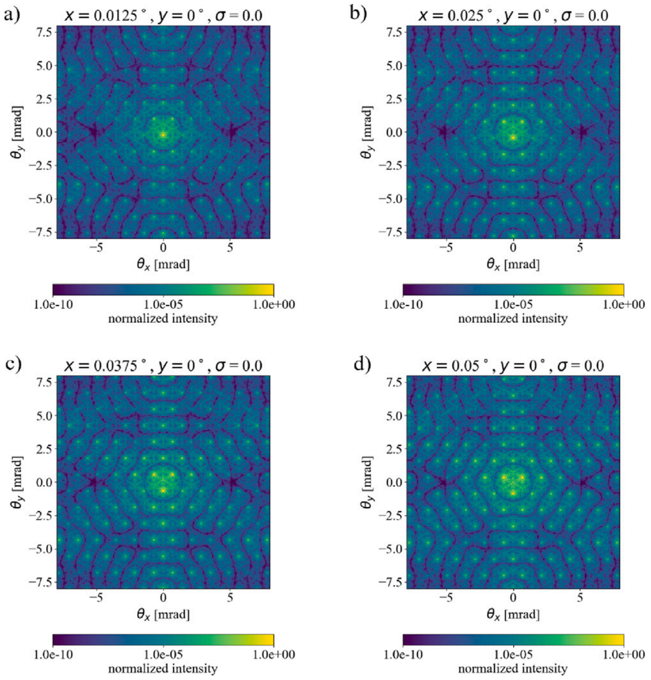

Fig. 10. Far-field diffraction patterns of an ideal tilted hexagonal array consisting of hexagonal sub-apertures. (a) FFDP at 0.0125° tilt, (b) FFDP at 0.025° tilt, (c) FFDP at 0.0375° tilt, (d) FFDP at 0.05° tilt. x and y in the header specify the tilt around the x-axis respectively the y-axis and σ the standard deviation of a Gaussian distribution in rad.

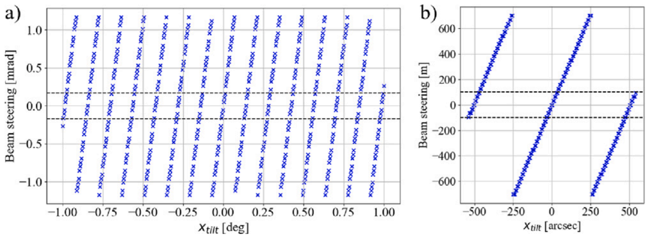

Fig. 11. Beam steering during SLR for a coherent retroreflective array (10 mm diameter, 500 μm radius of sub-aperture). (a) Angular displacement in an angle range of ±1°, (b) Actual beam displacement at the ground station of a satellite at 600 km altitude. The dashed line indicates the footprint of the beam on the ground.

the minimum of a single unit (or incoherent case) (See Fig. 10(c)). As the angle increases further, the initial central maximum shifts towards the edge and eventually fades out after the full gradient of 2π has been traversed. Subsequently, increasing the angle periodically produces the same result, causing the described phenomenon to repeat. Additional changes (not observable in the featured figures) appear for high angles since the effective apertures become oval in shape. Since, the full gradient is achieved when the edge is shifted in the z-direction by the length of a wavelength, these effects are highly sensitive to the slightest tilt (ultimately depending of the size of the array). This can also be seen in Fig. 11(a), which shows that in this case, it is already repeated several times between −1° and +1°. Fig. 10(b) shows an extract of the first full gradient which emerges between 0 and 250 arcsec. For better comprehensibility, this shows that the beam is steered up to approximately 650 m of the ground station, while the maxima only has a footprint of 200 m in diameter (marked as dashed line in Fig. 11(b)).

References

[1] M.R. Pearlman, C.E. Noll, E.C. Pavlis, F.G. Lemoine, L. Combrink, J.J. Degnan, G. Kirchner, U. Schreiber, The ILRS: approaching 20 years and planning for the future, J. Geod. 93 (11) (2019) 2161–2180, http://dx.doi.org/10.1007/s00190-019-01241-1.

[2] D. Hampf, W. Riede, N. Bartels, E. Schafer, P. Wagner, A path towards low-cost, high-accuracy orbital object monitoring, in: T. Flohrer, S. Lemmens, F. Schmitz (Eds.), 8Th European Conference on Space Debris, 2021.

[3] R.T. Howard, T.C. Bryan, L.L. Brewster, J.E. Lee, Proximity operations and docking sensor development, in: 2009 IEEE Aerospace Conference, IEEE, 2009, pp. 1–10, http://dx.doi.org/10.1109/aero.2009.4839574.

[4] M. Pfennigbauer, J. Pereira do Carmo, B. Moebius, Imaging lidar technology: development of a 3D-lidar elegant breadboard for rendezvous and docking, test results, and prospect to future sensor application, in: N. Kadowaki (Ed.), International Conference on Space Optics — ICSO 2010, SPIE, 2017, p. 103, http://dx.doi.org/10.1117/12.2309246.

[5] H. Krag, M. Lindsay, M.A. Skinner, Y. Kitazawa, P. Marzioli, Innovative methods for trackability and identification improvement of small objects for space traffic management, Acta Astronaut. 225 (2024) 1012–1018, http://dx.doi.org/10.1016/j.actaastro.2024.10.004.

[6] P. Sauer, G. Kirchner, M. Michel, V. Neumann, C. Weber, D. Auth, R. Bertrand, S. Breuer, Examining retro-reflective foils for use in smallsat applications and space debris laser ranging, in: 72Nd International Astronautical Congress, IAC, 2021.

[7] TU Darmstadt Space Technology e.v., TRACE CubeSat team - payload & research, 2004, URL https://www.tudsat.space/trace-payload-and-research, (Accessed 16 January 2025).

[8] D.C. Ullery, S. Soleymani, A. Heaton, J. Orphee, L. Johnson, R. Sood, P. Kung, S.M. Kim, Strong solar radiation forces from anomalously reflecting metasurfaces for solar sail attitude control, Sci. Rep. 8 (2018) http://dx.doi.org/10.1038/s41598-018-28133-2.

[9] K. Sun, C.A. Riedel, Y. Wang, A. Urbani, M. Simeoni, S. Mengali, M. Zalkovskij, B. Bilenberg, C.H. de Groot, O.L. Muskens, Metasurface optical solar reflectors using AZO transparent conducting oxides for radiative cooling of spacecraft, ACS Photonics 5 (2) (2017) 495–501, http://dx.doi.org/10.1021/acsphotonics.7b00991.

[10] G. Minatti, M. Faenzi, E. Martini, F. Caminita, P. De Vita, D. Gonzalez-Ovejero, M. Sabbadini, S. Maci, Modulated metasurface antennas for space: Synthesis, analysis and realizations, IEEE Trans. Antennas and Propagation 63 (4) (2015) 1288–1300, http://dx.doi.org/10.1109/tap.2014.2377718.

[11] S.E. Dean, J. Munro, N. Li, R. Sharp, D.N. Neshev, A.A. Sukhorukov, Metasurfaces-based polarisation imaging systems for small form-factor satellites, in: K.F. MacDonald, A.V. Zayats, I. Staude (Eds.), Metamaterials XIV, Proc. SPIE 12990, 2024, http://dx.doi.org/10.1117/12.3022227.

[12] X. Zhu, V. Hsu, J. Kahn, Optical modeling of MEMS corner cube retroreflectors with misalignment and nonflatness, IEEE J. Sel. Top. Quantum Electron. 8 (1) (2002) 26–32, http://dx.doi.org/10.1109/2944.991396.

[13] J.J. Degnan, Millimeter accuracy satellite laser ranging: a review, in: D.E. Smith, D.L. Turcotte (Eds.), Contributions of Space Geodesy To Geodynamics: Technology, in: Geodynamics Series, vol. 25, American Geophysical Union, 1993, pp. 133–162, http://dx.doi.org/10.1029/gd025.

[14] D.A. Arnold, Method of Calculating Retroreflector-Array Transfer Functions, Contractor Report (CR) NASA-CR-157932, Smithsonian Astrophysical Observatory, Cambridge, MA, United States, 1978.

[15] G. Brooker, Modern Classical Optics, eighth ed., in: Oxford Master Series in Physics, Oxford Univ. Press, Oxford, 2011.

[16] E. Brinksmeier, R. Gläbe, C. Flucke, Manufacturing of molds for replication of micro cube corner retroreflectors, Prod. Eng. 2 (1) (2008) 33–38, http://dx.doi.org/10.1007/s11740-008-0082-8.

[17] N. Milliken, B. Hamilton, S. Hussein, O.R. Tutunea-Fatan, E. Bordatchev, Enhanced bidirectional ultraprecise single point inverted cutting of right triangular prismatic retroreflectors, Precis. Eng. 52 (2018) 158–169, http://dx.doi.org/10.1016/j.precisioneng.2017.12.002.

[18] N. Milliken, O.R. Tutunea-Fatan, E.V. Bordatchev, Analysis of surface quality during fabrication of automotive retroreflectors, Meas. 134 (2019) 649–657, http://dx.doi.org/10.1016/j.measurement.2018.11.011.

[19] E. Brinksmeier, R. Gläbe, L. Schönemann, Diamond micro chiseling of large-scale retroreflective arrays, Precis. Eng. 36 (4) (2012) 650–657, http://dx.doi.org/10.1016/j.precisioneng.2012.06.001.

[20] M. Feiling, Feasibility Study of Using Retroreflective Foils for Satellite Laser Ranging (Master's thesis), Justus-Liebig-Universitaet Giessen, 2024.

[21] 3M Deutschland GmbH, Reflexfolien: Aufbau und vergleich, 2004, URL https://www.reflexfolie.de/media/pdf/47/6d/7e/3M-Reflexfolien_Aufbau_Vergleich.pdf, (Accessed 07 January 2025).

[22] International Laser Ranging Service, Current missions, 2025, URL https://ilrs.gsfc.nasa.gov/missions/satellite_missions/current_missions/index.html, (Accessed 13 March 2025).

[23] H.-H. Hsiao, C.H. Chu, D.P. Tsai, Fundamentals and applications of metasurfaces, Small Methods 1 (4) (2017) http://dx.doi.org/10.1002/smtd.201600064.

[24] A. Arbabi, E. Arbabi, Y. Horie, S.M. Kamali, A. Faraon, Planar metasurface retroreflector, Nat. Photonics 11 (7) (2017) 415–420, http://dx.doi.org/10.1038/nphoton.2017.96.

[25] H. Suo, J. Ding, X. Tang, L.K. Chin, C. Qian, Z. Zhu, Y. Liao, Z. Fan, Y. Yu, Wide-angle and high-efficiency flat retroreflector, Opt. Express 30 (15) (2022) 27249–27258, http://dx.doi.org/10.1364/oe.461210.

[26] L. Zhang, S. Chang, X. Chen, Y. Ding, M.T. Rahman, Y. Duan, M. Stephen, X. Ni, High-efficiency, 80 mm aperture metalens telescope, Nano Lett. 23 (1) (2022) 51–57, http://dx.doi.org/10.1021/acs.nanolett.2c03561.

[27] D. Hampf, F. Niebler, T. Meyer, W. Riede, The miniSLR: a low-budget, high-performance satellite laser ranging ground station, J. Geod. 98 (1) (2024) http://dx.doi.org/10.1007/s00190-023-01814-1.

[28] W.-L. Hsu, Y.-C. Chen, S.P. Yeh, Q.-C. Zeng, Y.-W. Huang, C.-M. Wang, Review of metasurfaces and metadevices: Advantages of different materials and fabrications, Nanomater. 12 (12) (2022) 1973, http://dx.doi.org/10.3390/nano12121973.

[29] J.-S. Park, S. Zhang, A. She, W.T. Chen, P. Lin, K.M.A. Yousef, J.-X. Cheng, F. Capasso, All-glass, large metalens at visible wavelength using deep-ultraviolet projection lithography, Nano Lett. 19 (12) (2019) 8673–8682, http://dx.doi.org/10.1021/acs.nanolett.9b03333.

[30] B. Wu, A. Kumar, Extreme ultraviolet lithography: A review, J. Vac. Sci. Technol. B: Microelectron. Nanometer. Struct. Process. Meas. Phenom. 25 (6) (2007) 1743–1761, http://dx.doi.org/10.1116/1.2794048.

[31] G. Yoon, T. Tanaka, T. Zentgraf, J. Rho, Recent progress on metasurfaces: applications and fabrication, J. Phys. D: Appl. Phys. 54 (38) (2021) 383002, http://dx.doi.org/10.1088/1361-6463/ac0faa.

[32] J. Kästel, J. Speiser, Laser-based space debris removal: design guidelines for coherent coupling power transmission, in: H. Ackermann, W.L. Bohn, D.H. Titterton (Eds.), High-Power Lasers 2016: Technology and Systems, Vol. 9990, SPIE, 2016, 99900L, http://dx.doi.org/10.1117/12.2239772.

[33] N. Bartels, P. Allenspacher, S. Bauer, B. Rödiger, F. Sproll, W. Riede, Design and qualification of a recessed satellite cornercube retroreflector for ground-based attitude verification via satellite laser ranging, CEAS Space J. 11 (4) (2019) 391–403, http://dx.doi.org/10.1007/s12567-019-00255-x.

[34] A. Bacchetta, M. Saponara, A. Torasso, G. Saavedra Criado, B. Girouart, The Euclid AOCS science mode design, CEAS Space J. 7 (2) (2015) 71–85, http://dx.doi.org/10.1007/s12567-015-0084-2.

[35] C. Fuchs, F. Moll, D. Giggenbach, C. Schmidt, J. Keim, S. Gaisser, OSIRISv1 on flying laptop: Measurement results and outlook, in: 2019 IEEE International Conference on Space Optical Systems and Applications, ICSOS, IEEE, 2019, pp. 1–5, http://dx.doi.org/10.1109/icsos45490.2019.8978984.

[36] C. Schmidt, B. Rodiger, J. Rosano, C. Papadopoulos, M.-T. Hahn, F. Moll, C. Fuchs, DLR's optical communication terminals for CubeSats, in: 2022 IEEE International Conference on Space Optical Systems and Applications, ICSOS, IEEE, 2022, pp. 175–180, http://dx.doi.org/10.1109/icsos53063.2022.9749735.

[37] J. Wang, Y. Zhao, B. Geng, Impact of atmospheric turbulence on the signal intensity of the laser ranging echo of space debris, Appl. Opt. 63 (36) (2024) 9268, http://dx.doi.org/10.1364/ao.535105.

[38] M. Fruit, A.I. Gusarov, D.B. Doyle, G.J. Ulbrich, Radiation impact on spaceborne optics: the dose coefficients approach, in: E.W. Taylor, F. Berghmans (Eds.), Photonics for Space and Radiation Environments, Vol. 3872, Proc. SPIE, 1999, pp. 60–71, http://dx.doi.org/10.1117/12.373286.

[39] M. Fruit, A.I. Gusarov, D.B. Doyle, Measuring space radiation impact on the characteristics of optical glasses: measurement results and recommendations from testing a selected set of materials, in: E.W. Taylor (Ed.), Photonics for Space Environments VIII, Vol. 4823, Proc. SPIE, 2002, pp. 132–141, http://dx.doi.org/10.1117/12.452255.

[40] E. Grossman, I. Gouzman, Space environment effects on polymers in low earth orbit, Nucl. Instrum. Methods Phys. Res. Sect. B: Beam Interact. Mater. At. 208 (2003) 48–57, http://dx.doi.org/10.1016/s0168-583x(03)00640-2.

[41] S. Pellicori, Coatings used in space, Coat. Mater. News 26 (2) (2017).

[42] D. de Jong, J. Karst, D. Ludescher, M. Floess, S. Moell, K. Dirnberger, M. Hentschel, S. Ludwigs, P.V. Braun, H. Giessen, Electrically switchable metallic polymer metasurface device with gel polymer electrolyte, Nanophotonics 12 (8) (2023) 1397–1404, http://dx.doi.org/10.1515/nanoph-2022-0654.

[43] N. Bartels, P. Allenspacher, D. Hampf, B. Heidenreich, D. Keil, E. Schafer, W. Riede, Space object identification via polarimetric satellite laser ranging, Commun. Eng. 1 (1) (2022) http://dx.doi.org/10.1038/s44172-022-00003-w.

[44] D.L. Bakker, G. Castro do Amaral, E. Di Iorio, L.W. Feenstra, I. Ferrario, B. Perlingeiro, F. Silvestri, Satellite license plate: passive and compact optical spectrally-based identification method for satellites, Commun. Eng. 3 (1) (2024) http://dx.doi.org/10.1038/s44172-024-00188-2.

[45] C. Song, Z. Liang, H. Lin, Passive attitude estimation of spacecraft based on multiretroreflector differential satellite laser ranging, IEEE Trans. Geosci. Remote Sens. 62 (2024) 1–17, http://dx.doi.org/10.1109/tgrs.2024.3491099.